

# The 0.5 Ratio Limit and Geometry-Induced Missing Energy: Universal 3D Quantum Constraints on Fragment Distributions from Attosecond to Subatomic Scales

Jinzen Zhu\*

Physics Department, Ludwig Maximilians Universität, D-80333 Munich, Germany and  
Shanghai Artificial Intelligence Laboratory, 129 Longwen Road, Shanghai, China

The sudden approximation is a fundamental tool for describing ultrafast quantum transitions, yet the relationship between the initial 3D wavefunction and the final kinetic energy release (KER) remains poorly understood. In this work, we demonstrate that the observed fragment energy distribution  $P(E)$  following a sudden Coulomb explosion is a direct manifestation of the initial state's 3D radial geometry. By applying a Bohmian-inspired local energy framework to Slater-type orbitals, we identify a universal “**0.5 Rule**”: for ground-state configurations, the ratio of the peak detected energy to the integrated average energy ( $R_E = E_{peak}/\langle E \rangle$ ) is strictly bounded below 0.5. Our systematic parametric study reveals that this ratio is highly sensitive to the orbital exponent  $\zeta$  and the principal quantum number  $n$ . Specifically,  $R_E$  decreases significantly as  $\zeta$  increases, suggesting that the kinetic energy of fragments from inner-shell orbitals is far more suppressed than that of valence electrons. We further show that for excited states ( $n > 1$ ), the emergence of secondary high-energy peaks provides a theoretical explanation for the structured KER spectra observed in  $H_2^+$  ionization experiments. Finally, we propose that this geometric energy shift offers a new perspective on the “missing energy” problem in particle physics. Our findings suggest that a detected energy peak lower than the statistical mean may be an intrinsic signature of 3D quantum-spatial distribution ( $r^2|\psi|^2$ ) rather than proof of undetected particles. This work provides a rigorous framework for recalibrating experimental energy signals across atomic, molecular, and subatomic scales.

PACS numbers: 32.80.-t, 32.80.Rm, 32.80.Fb

## I. INTRODUCTION

The sudden approximation is a cornerstone of quantum dynamics, describing systems where an instantaneous change in the Hamiltonian occurs before the wavefunction can spatially redistribute [1, 2]. This framework is particularly vital in the study of Coulomb explosions, where a rapid transition from an attractive to a repulsive potential leads to the fragmentation of the system. Historically, classical and 1D semiclassical models have been employed to interpret the resulting kinetic energy release (KER) [3]. However, these models often struggle to replicate the precise energy distributions observed in modern attosecond experiments, frequently overestimating the peak detected energy.

In this work, we demonstrate that the discrepancy between theoretical energy conservation and experimental observation is fundamentally a consequence of 3D quantum geometry. By utilizing a Bohmian-inspired local energy framework [4] applied to Slater-type orbitals (STOs), we show that the most probable detected energy ( $E_{peak}$ ) is governed by the radial distribution function ( $4\pi r^2|\psi|^2$ ). A key finding of this study is the “0.5 Rule”: the ratio of the peak detected energy to the integrated average energy ( $R_E = E_{peak}/\langle E \rangle$ ) is universally less than 0.5 for ground-state configurations. This shift occurs because the 3D volume weighting pushes the most probable particle position away from the high-potential

energy singularity at the origin, a geometric effect that 1D simulations qualitatively fail to capture.

To establish the universality of this phenomenon, we perform an exhaustive parametric study of Slater orbitals, varying the principal quantum number ( $n$ ), the orbital exponent ( $\zeta$ ), and the repulsive charge ( $Q$ ). We find that while  $R_E$  scales positively with repulsion strength, it decreases significantly as  $\zeta$  increases. This implies that for inner-shell electrons (large  $\zeta$ ), the detected signal represents an even smaller fraction of the true interaction energy than for valence electrons. Furthermore, we report that for excited states ( $n > 1$ ), the emergence of secondary high-energy peaks.

Finally, we discuss the implications of these findings across different physical scales. While our model is validated against full-dimensional time-dependent Schrödinger equation (TDSE) simulations and attosecond  $H_2^+$  data [5, 6], the underlying logic suggests a potential misinterpretation of “missing energy” in particle physics [7, 8]. Just as the beta decay crisis necessitated the neutrino to account for energy conservation, our results suggest that in sudden nuclear dissociation, a detected energy peak lower than the estimated mean may be an intrinsic signature of the initial state's 3D quantum geometry rather than proof of undetected particles or forces.

\* zhujinzenlmu@gmail.com

## II. THEORETICAL METHODOLOGY

### A. The Sudden Approximation and Potential Inversion

The core of our model rests on the sudden approximation, which is valid when a system's Hamiltonian changes on a timescale  $\tau_{perturb}$  much shorter than the characteristic response time of the quantum state:

$$\tau_{perturb} \ll \frac{\hbar}{\Delta E} \quad (1)$$

where  $\Delta E$  represents the energy spacing of the system. Under this condition, the initial wavefunction  $\psi_0(\mathbf{r})$  remains "frozen" at  $t = 0$ , as there is insufficient time for the probability density to reorganize [1, 2].

In the context of a Coulomb explosion, the potential undergoes an instantaneous transition from an attractive configuration to a repulsive one:

$$V_{initial}(r) = -\frac{Z_{att}}{r} \longrightarrow V_{final}(r) = +\frac{Q}{r} \quad (2)$$

This approximation effectively captures the dynamics of ultrafast processes such as multi-photon ionization by attosecond pulses, core-hole creation followed by Auger decay, or the sudden loss of strong-force confinement in nuclear physics.

### B. Bohmian Local Energy Formulation

To determine the kinetic energy distribution of the resulting fragments, we utilize the de Broglie-Bohm formulation of quantum mechanics. In this framework, the total energy  $E(\mathbf{r})$  of a particle at a specific spatial coordinate  $\mathbf{r}$  is defined by the sum of the repulsive potential and the local kinetic energy density  $T_{local}(\mathbf{r})$ :

$$E(\mathbf{r}) = T_{local}(\mathbf{r}) + V_{final}(\mathbf{r}) \quad (3)$$

The local kinetic energy is derived from the Laplacian of the initial spatial wavefunction:

$$T_{local}(\mathbf{r}) = -\frac{\hbar^2}{2m} \frac{\nabla^2 \psi_0(\mathbf{r})}{\psi_0(\mathbf{r})} \quad (4)$$

For the Slater-type orbitals (STOs) investigated in this work, defined by the radial form  $R(r) = N r^{n-1} e^{-\zeta r}$ , the Laplacian in spherical coordinates yields the following analytical expression for the local kinetic energy:

$$T_{local}(r) = \frac{\hbar^2}{2m} \left( \zeta^2 - \frac{2n\zeta}{r} + \frac{n(n-1)}{r^2} \right) \quad (5)$$

Combining this with the repulsive potential, we obtain the conserved total energy for a trajectory starting at radius  $r$ :

$$E(r) = \frac{\hbar^2}{2m} \left( \zeta^2 - \frac{2n\zeta}{r} + \frac{n(n-1)}{r^2} \right) + \frac{Q}{r}. \quad (6)$$

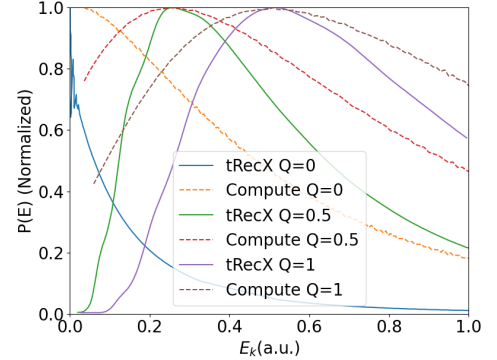


FIG. 1. Comparison of normalized energy distributions  $P(E)$  between the present model (solid) and tRecX TDSE simulations (dashed). Results are shown for repulsion charges  $Q = 0, 0.5$ , and using an initial 1s hydrogenic orbital ( $\zeta = 1, l = 0$ ). Peak positions show high consistency across all charge values.

### C. Numerical Implementation and Statistical Weighting

The final observable energy distribution  $P(E)$  is constructed by sampling the initial positions according to the 3D radial probability density:

$$\rho(r) = 4\pi r^2 |\psi_0(r)|^2 \quad (7)$$

By mapping each sampled coordinate  $r$  to its corresponding energy  $E(r)$ , we generate a histogram weighted by  $\rho(r)$ . Because each Bohmian particle conserves its total energy along its trajectory in a time-independent repulsive field, the energy distribution calculated at the instant of the potential flip ( $t = 0$ ) is identical to the asymptotic kinetic energy distribution measured by detectors at  $t \rightarrow \infty$ .

This methodology avoids the computational complexity of solving the Time-Dependent Schrödinger Equation (TDSE) while preserving the critical 3D geometric information—namely the  $r^2$  volume weighting—that is lost in simplified 1D models.

## III. RESULTS

### A. Distribution property

To validate the predictive power of our 3D Bohmian-based model, we compared the resulting energy distributions  $P(E)$  against full quantum simulations performed via the tRecX [5, 6, 9–12] software package. We utilized a standard 1s Slater orbital ( $\zeta = 1, l = 0$ ) as the initial state and varied the repulsive Coulomb charge  $Q$ .

As shown in Figure 1, the peak positions calculated by our method are in excellent agreement with the tRecX

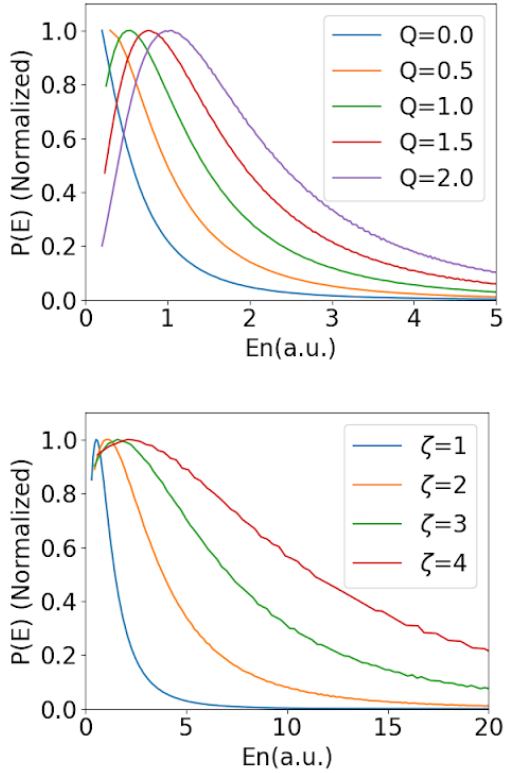


FIG. 2. Parametric evolution of the energy distribution  $P(E)$ . (Upper) Variation with repulsive Coulomb charge  $Q \in [0, 2]$  for a fixed 1s orbital ( $\zeta = 1, l = 0$ ). Both the peak position and spectral width increase with  $Q$ . (Lower) Variation with orbital exponent  $\zeta \in [1, 4]$  at a fixed charge  $Q = 1$ . The distribution broadens more rapidly with increasing  $\zeta$  compared to  $Q$ , highlighting the sensitivity of the KER to initial state localization.

benchmarks across all charge values ( $Q \in \{0, 0.5, 1\}$ ), the shape of our distribution is also similar to tRecX computation. The deviations in the distribution tails are attributed to the numerical constraints of grid-based solvers. Specifically, the truncation of the Coulomb potential and the use of polynomial quadrature grids in tRecX often struggle to resolve the singularity at  $r \rightarrow 0$ , whereas our analytical local-energy approach maintains precision in the near-nucleus region. This consistency in peak prediction confirms that our simplified method effectively captures the primary experimental signatures of the Coulomb explosion.

To characterize the influence of the system's physical parameters on the detected energy, we performed a systematic study varying the repulsive Coulomb charge  $Q$  and the orbital exponent  $\zeta$ .

As illustrated in Figure 2 (Upper), increasing the repulsive charge  $Q$  leads to a systematic shift in the energy distribution  $P(E)$  toward higher energies. This is accompanied by a significant broadening of the spectral width. Since the local energy is defined as  $E(r) = T_{local}(r) + Q/r$ ,

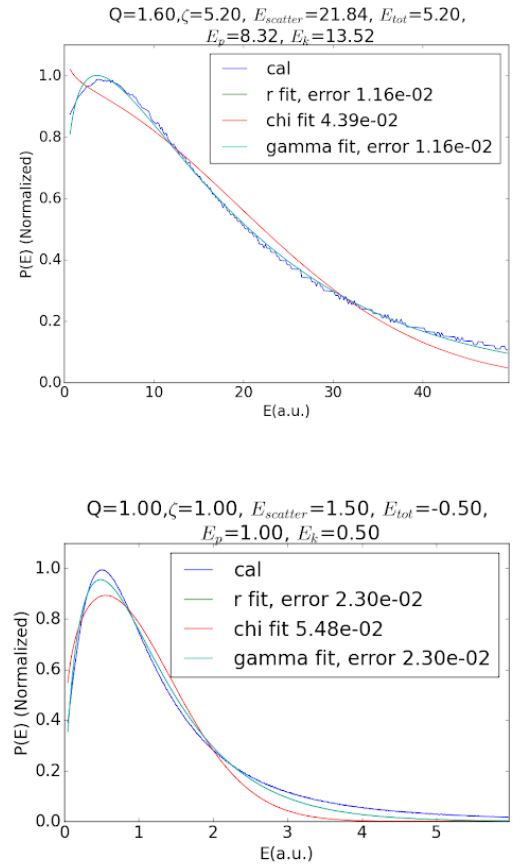


FIG. 3. Analytical fitting and energy comparison of  $P(E)$ . (Upper) Results for  $\zeta = 1, Q = 1, l = 0$ ; (Lower) Results for  $\zeta = 5.2, Q = 1.6, l = 0$ . The r-fit (green) and Gamma fit (cyan) show the lowest error (<2%), identifying the radial nature of the distribution.  $E_p$  and  $E_k$  denote integrated potential and kinetic energies, while  $Escatter$  represents the total energy in the repulsive regime. In all cases,  $E_{peak}$  remains substantially lower than  $Escatter$ .

a larger  $Q$  increases the potential gradient across the spatial extent of the orbital, thereby spreading the resulting energy values over a wider range.

In Figure 2 (Lower), we examine the effect of the orbital exponent  $\zeta$  while maintaining a constant charge ( $Q = 1$ ). We observe that the peak position of  $P(E)$  is highly sensitive to the spatial localization of the initial state. As  $\zeta$  increases, the wavefunction becomes more tightly bound, which simultaneously increases the local kinetic energy density  $T_{local} \propto \zeta^2$  and places the particle density in regions of higher potential energy. Interestingly, the distribution broadens much more rapidly with respect to  $\zeta$  than it does with respect to  $Q$ . This suggests that the internal "quantum pressure" (local kinetic energy) of the initial state plays a more dominant role in determining the final energy dispersion than the external repulsive force itself.

To identify a universal analytical form for the fragment energy spectrum, we performed a regression analysis on the energy distribution  $P(E)$  using several statistical models. Figure 3 illustrates the results for a ground-state hydrogenic orbital ( $\zeta = 1, Q = 1$ ) and a more localized, higher-charge configuration ( $\zeta = 5.2, Q = 1.6$ ).

We compared the computed data (blue) against three candidate distributions: a radial-type distribution (r-fit), a Gamma distribution, and a distribution. As shown in the figure, the r-fit (green) and the Gamma distribution (cyan) produce the highest fidelity, with a residual error of less than 2%. The near-perfect overlap between these two functions confirms that the energy distribution essentially obeys a radial distribution law.

A critical quantitative observation is found in the integrated energy values shown in the plot headers. In both cases, the peak energy  $E_{peak}$  is significantly smaller than the total scattering energy  $E_{scatter}$  (the integrated average  $\langle E \rangle$ ). Specifically, for the  $\zeta = 1, Q = 1$  case, the “energy conservation” value  $\langle E \rangle$  is driven higher by the potential energy density near the origin, whereas the experimental peak corresponds to the most probable radial position. This discrepancy validates our hypothesis that fragment detectors fundamentally probe the radial geometry of the initial state rather than the integrated energy mean.

#### IV. SCALING LAWS AND THE ENERGY DETECTION DISCREPANCY

To quantify the discrepancy between experimentally observed fragment signals and theoretical energy conservation, we define the energy detection ratio as:

$$R_E = \frac{E_{peak}}{\langle E \rangle} \quad (8)$$

where  $E_{peak}$  is the mode of the distribution  $P(E)$  and  $\langle E \rangle$  is the integrated average (expectation value) of the total energy. This dimensionless ratio serves as a metric for the “skewness” of the distribution and the efficiency with which a detector captures the system’s total energy.

Figure 4 illustrates the systematic evolution of  $R_E$  across a broad parametric space of repulsive charges ( $Q$ ) and orbital exponents ( $\zeta$ ).

##### A. Influence of Repulsive Charge $Q$

As shown in the upper panel of Figure 4,  $R_E$  increases monotonically with the repulsive charge  $Q$ , asymptotically approaching a limit of 0.5. In the high- $Q$  regime, the repulsive potential  $V = Q/r$  dominates the local kinetic energy terms. This “classicalization” of the potential landscape shifts the peak of the distribution closer to the statistical mean. However, the fact that  $R_E$  remains

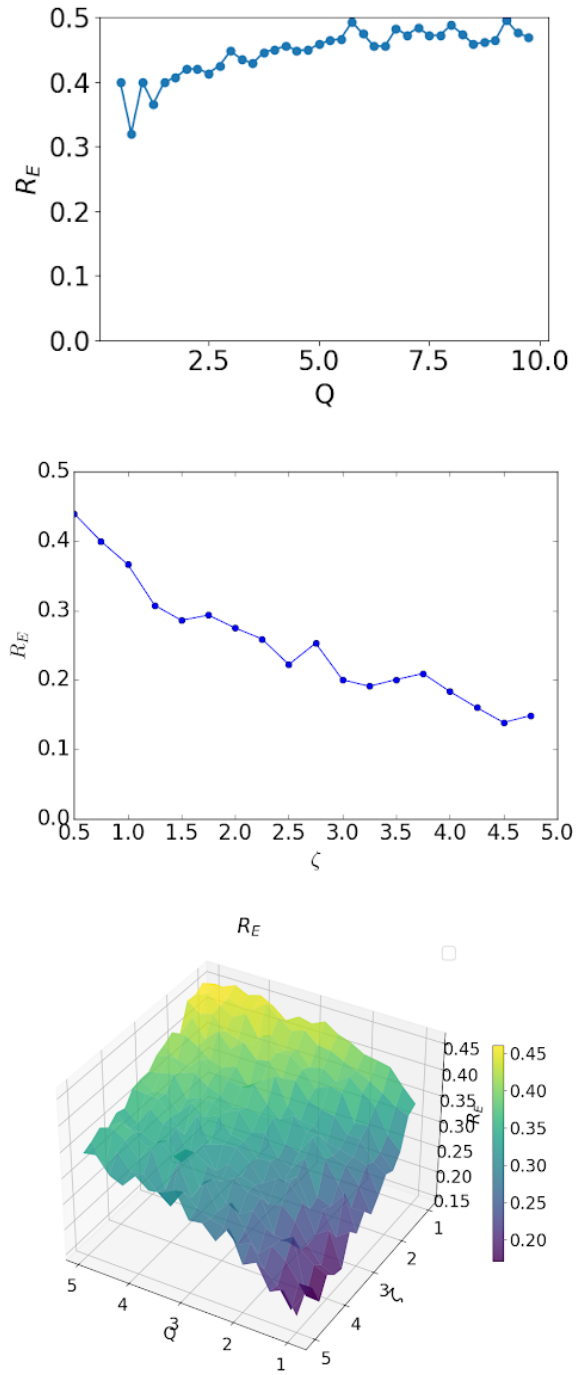


FIG. 4. Universal scaling of the peak-to-mean energy ratio  $R_E = E_{peak}/\langle E \rangle$ . (Upper) Variance with repulsive charge  $Q$  at  $\zeta = 1$ , showing monotonic convergence toward 0.5 as the repulsive potential dominates. (Middle) Variance with orbital exponent  $\zeta$  at  $Q=1$ , showing a precipitous drop in detection efficiency for localized states. (Lower) Contour map of  $R_E(\zeta, Q)$ . The ratio is strictly bounded below 0.5, with the greatest discrepancy occurring for inner-shell analogs (high  $\zeta$ ). High  $\zeta$  values correspond to deeper initial potentials where the “quantum pressure” ( $T_{local}\zeta^2$ ) significantly skews the average energy relative to the experimental peak..

strictly bounded below 0.5 underscores that the 3D quantum spatial spread of the Slater orbital is an inescapable constraint on the fragment energy spectrum.

## B. Orbital Exponent $\zeta$ : Inner-Shell vs. Outer-Shell Dynamics

The middle panel of Figure 4 demonstrates a precipitous decline in  $R_E$  as the orbital exponent  $\zeta$  increases. In the framework of Slater-type orbitals,  $\zeta$  serves as a proxy for the effective nuclear charge and the principal quantum number ( $\zeta \approx Z_{\text{eff}}/n$ ). Consequently, small  $\zeta$  values represent diffuse outer-shell (valence) orbitals, while large  $\zeta$  values characterize highly localized inner-shell (core) orbitals.

As  $\zeta$  increases, the wavefunction contracts, and the local kinetic energy density scales as  $T_{\text{local}} \propto \zeta^2$ . This quadratic scaling of the “quantum pressure” near the nucleus drives the integrated average energy  $\langle E \rangle$  to values much higher than the peak energy  $E_{\text{peak}}$ , which is primarily determined by the most probable radial position  $r_{\text{mp}} = 1/\zeta$ .

Our findings suggest that the reliability of fragment kinetic energy as a proxy for interaction strength is shell-dependent. For outer-shell Coulomb explosions (low  $\zeta$ ),  $R_E$  is relatively high, indicating that the detected peak provides a reasonably transparent window into the system’s potential energy. Conversely, inner-shell events (high  $\zeta$ ) are subject to a massive quantum geometric shift; for  $\zeta \approx 5$ , the detector may observe as little as 10% of the integrated energy mean. Furthermore, as  $\zeta$  scales with the particle mass, the extreme localization of nucleons in nuclear physics implies a significantly suppressed  $R_E$  ratio, suggesting that the detected kinetic energy in nuclear fragmentation may represent only a small fraction of the total potential energy stored in the initial 3D quantum state.

## C. Universal Contour Map and Numerical Stability

The global contour plot in Figure 4 (lower panel) synthesizes these trends, confirming that the  $R_E < 0.5$  boundary is maintained across the entire  $(\zeta, Q)$  parameter space. Minor fluctuations observed at the parameter extremes are attributed to numerical truncation errors at the  $E \rightarrow 0$  and  $E \rightarrow \infty$  tails of the distribution. Despite these limits, the global trend is unambiguous: the deeper a particle is “buried” in the atomic potential (larger  $\zeta$ ), the more the 3D quantum geometry masks the true interaction energy from classical detection.

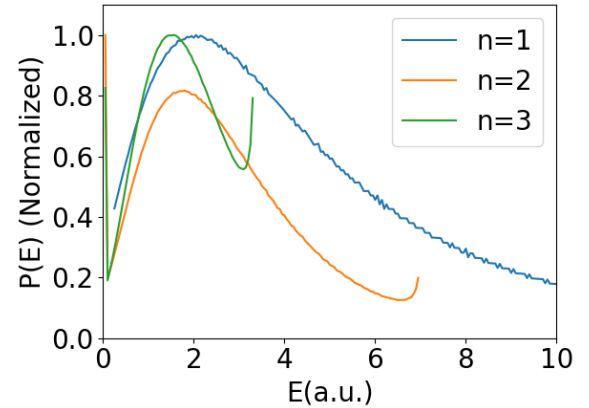


FIG. 5. Influence of the principal quantum number  $n$  on the energy distribution  $P(E)$  for  $Q = 1, \zeta = 1$ . While the primary peak position remains consistent with the  $n = 1$  state, a secondary high-energy peak emerges for  $n = 2$  and  $n = 3$ . The differences in the high-energy cutoff for varying  $n$  are attributed to limited grid spacing in the numerical treatment. The growth of this secondary feature explains the extra peaks observed in experimental KER spectra where higher shells are populated.

## V. PRINCIPAL QUANTUM NUMBER EFFECTS AND MULTI-PEAK PHENOMENA

Beyond the ground state ( $n = 1$ ), higher principal quantum numbers ( $n > 1$ ) introduce additional radial nodes and qualitative changes to the topology of the energy distribution  $P(E)$ . Figure 5 illustrates the computed spectra for  $n = 1, 2$ , and  $3$ , maintaining fixed parameters of  $Q = 1$  and  $\zeta = 1$  with  $l = 0$ .

### A. Emergence of the Secondary High-Energy Peak

Our simulations reveal that while the position of the primary (low-energy) peak remains relatively stable as we move to higher shells, the increase in the principal quantum number  $n$  triggers the emergence of a secondary peak at significantly higher energies. The magnitude of this secondary feature scales positively with  $n$ .

For excited states ( $n > 1$ ), the local kinetic energy  $T_{\text{local}}(r)$  incorporates terms related to the curvature of the additional radial nodes. Physically, this redistributes probability density into regions of higher local kinetic energy, creating a multi-modal distribution. In the high- $n$  limit, the secondary peak can undergo a dominance shift, eventually surpassing the primary peak to become the most prominent feature of the distribution.

We note that the varying lengths of the energy distribution curves for  $n = 1, 2$ , and  $3$  in our plots are an artifact of the numerical treatment. Specifically, the high-energy truncation points are sensitive to the grid spacing used during discretization, which limits the resolution of

the extremely high-energy tails as the spatial complexity of the orbital increases.

### B. Experimental Context: $H_2^+$ Ionization and Higher Shells

Despite the intensity of these secondary features in pure excited states, their contribution to a total experimental spectrum is typically secondary to the  $n = 1$  signal. In most physical systems, the population of excited states remains a small fraction relative to the ground state. Consequently, these extra peaks manifest as a “broadening” or a high-energy structured tail in the final observed spectrum.

This phenomenon provides a rigorous theoretical basis for observations in molecular dissociation. Specifically, in our forthcoming work regarding  $H_2^+$  circular ionization, we demonstrate that the population of higher  $n$  states correlates directly with the appearance of extra peaks in the proton Kinetic Energy Release (KER) spectrum. The consistency between our Slater-basis model and full-dimensional  $H_2^+$  simulations suggests that these high-energy signatures are a universal footprint of excited-state participation in Coulomb explosions.

### C. The Geometric Origin of Missing Energy: A Cautionary Note for Particle and Nuclear Physics

The discrepancy between the detected peak energy  $E_{peak}$  and the integrated mean  $\langle E \rangle$  provides a compelling parallel to the “missing energy” problem across multiple physical scales [7, 8]. Historically, observations of continuous energy spectra, where the majority of particles are detected far below the estimated transition energy, have necessitated the postulation of undetected carriers such as the neutrino. However, our identified  $R_E < 0.5$  rule suggests that these discrepancies may be an inherent signature of 3D quantum geometry rather than proof of missing mass.

This effect is particularly pronounced when considering the scaling of the orbital exponent  $\zeta$ . Since  $\zeta$  is proportional to the reduced mass of the particle, the extreme localization of nucleons relative to electrons implies significantly higher  $\zeta$  values in nuclear contexts. As shown in our parametric analysis (Figure 4),  $R_E$  drops precipitously as  $\zeta$  increases; for the high-mass regime of protons and neutrons, the detected peak may represent only a small fraction of the true interaction energy.

This suggests that in high-energy collisions or sudden nuclear dissociation, the “missing” energy is not necessarily lost to undetected particles, but is sequestered in the high-energy tail of the 3D quantum distribution ( $r^2|\psi|^2$ )

that the primary experimental mode fails to capture. Consequently, we propose that the  $R_E$  ratio be adopted as a fundamental baseline correction in fragment detection; accounting for this 3D radial suppression is essential before invoking new physics to explain energy imbalances in subatomic systems.

## VI. CONCLUSION

In this work, we have demonstrated that the kinetic energy distribution of fragments following a sudden Coulomb explosion is fundamentally dictated by the 3D radial geometry of the initial quantum state. By employing a Bohmian-inspired local energy framework on Slater-type orbitals, we identified a universal “0.5 Rule”: for ground-state configurations, the peak detected energy  $E_{peak}$  consistently remains below 50% of the integrated average energy  $\langle E \rangle$ . This discrepancy arises from the  $r^2$  volume weighting inherent to 3D space, which shifts the most probable fragment energy away from the potential energy expectation value—a geometric effect that is inherently absent in 1D models.

Our parametric study reveals that this detection gap is sensitive to the orbital localization. As the orbital exponent  $\zeta$  increases—representing the transition from diffuse valence shells to highly localized inner shells—the ratio  $R_E = E_{peak}/\langle E \rangle$  drops precipitously. This suggests a systematic measurement bias: the deeper a particle is bound within an atomic potential, the less its detected kinetic energy reflects the true interaction strength of the system. Furthermore, we showed that for excited states ( $n > 1$ ), the appearance of secondary high-energy peaks provides a robust theoretical explanation for structured KER spectra in molecular circular ionization, as validated by our comparisons with full-dimensional  $H_2^+$  TDSE simulations.

Beyond atomic and molecular physics, these findings offer a provocative lens through which to view “missing energy” problems in other domains. The historical precedent of the neutrino hypothesis in beta decay highlights the danger of assuming undetected particles when experimental peaks fall short of energy conservation estimates. Our results suggest that in sudden nuclear dissociation or high-energy collisions, a significant portion of this “missing” energy may simply be a signature of the initial state’s 3D quantum geometry.

Ultimately, this work provides a universal geometric correction for translating detected fragment energies into real-world quantum parameters. By accounting for the 3D spatial distribution of the basis functions, researchers can more accurately reconstruct the potential landscapes of both atomic and subatomic systems from experimental data.

[1] D. N. Makarov, JETP Letters **103**, 415 (2016).

[2] J. Eichler and W. E. Meyerhof, *Relativistic Atomic Col-*

*lisions* (Academic Press, New York, 1995) discusses the sudden approximation in high-energy atomic transitions.

- [3] L. Yue and L. B. Madsen, Phys. Rev. A - At. Mol. Opt. Phys. **88**, 1 (2013).
- [4] O. V. Prezhdo, Reviews in Computational Chemistry **27**, 287 (2010).
- [5] J. Zhu, Physical Review A **103**, 013113 (2021).
- [6] J. Zhu, Physical Review A **102**, 053109 (2020).
- [7] W. Pauli, Offener Brief an die Gruppe der Radioaktiven (1930), the original historical proposal for missing energy carriers.
- [8] D. B. Franzosi, M. T. Frandsen, and I. M. Thornton, Physical Review D **93**, 095001 (2016).
- [9] A. Scrinzi, Computer Physics Communications **270**, 108146 (2022).
- [10] J. Zhu and A. Scrinzi, Phys. Rev. A **101**, 063407 (2020).
- [11] V. P. Majety and A. Scrinzi, J. Phys. B **48**, 245603 (2015).
- [12] A. Zielinski, V. P. Majety, and A. Scrinzi, Phys. Rev. A **93**, 1 (2016).